Electronic Supplementary Material (ESI) for Journal of Materials Chemistry A.
This journal is © The Royal Society of Chemistry 2016

Supporting Information

Layer-by-layer assembly of nitrogen-doped graphene quantum dots monolayer decorated one-dimensional semiconductor nanoarchitectures for solar-driven water splitting

Zhiping Zeng, Fang-Xing Xiao*, Xuchun Gui, Rong Wang, Bin Liu*, Timothy Thatt Yang Tan*

Dr. Z. Zeng, Dr. F. X. Xiao, Prof B. Liu, Prof. T. T. Y. Tan
School of Chemical and Biomedical Engineering
Nanyang Technological University
Singapore 639798, Singapore
E-mail: fangxing2010@gmail.com (F. X. Xiao), liubin@ntu.edu.sg (B. Liu), tytan@ntu.edu.sg (T. T. Y. Tan)
Dr. Z. Zeng, Prof. R. Wang
Singapore Membrane Technology Center
Nanyang Environment and Water Research Institute
Interdisciplinary Graduate School
Nanyang Technological University
Singapore 637141, Singapore
Prof. X. Gui
State Key Lab of Optoelectronic Materials and Technologies
School of Electronics and Information Technology
Sun Yat-sen University, Guangzhou 510275, China

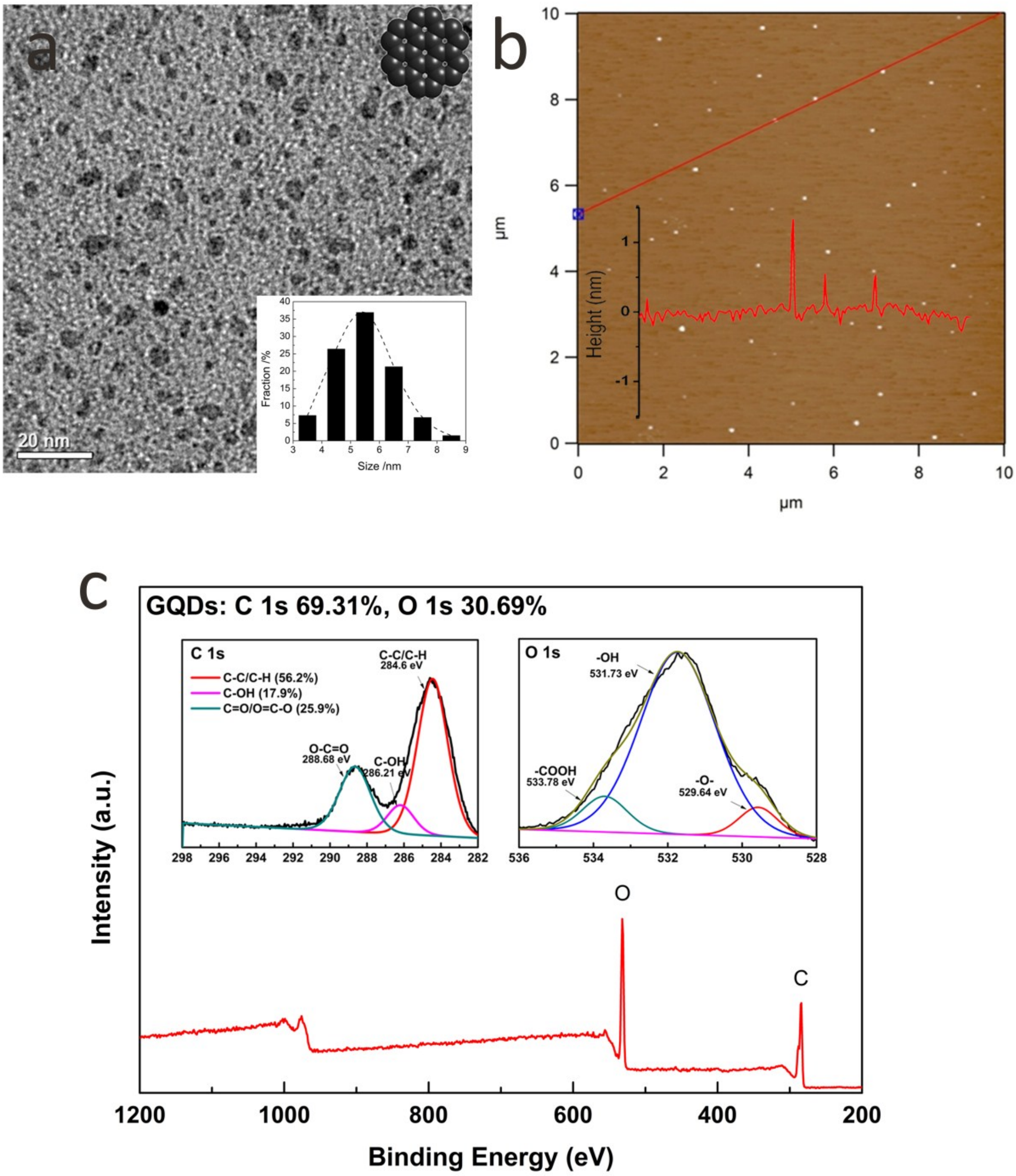

Fig. S1 (a) TEM images with size distribution histogram in the inset, (b) AFM image of GQDs, and (c) survey and high-resolution C 1s and O 1s spectra of GQDs.

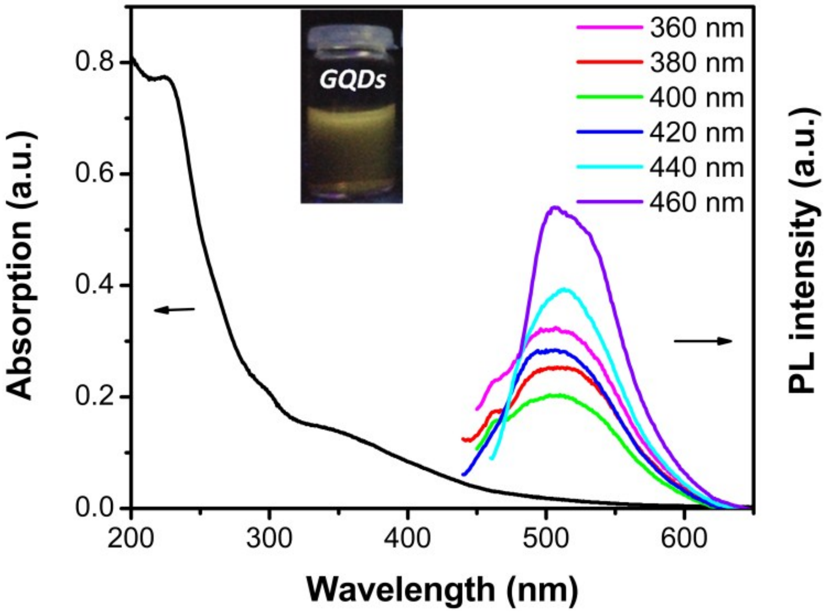

Fig. S2 UV-vis absorption spectrum and PL spectra of GQDs aqueous solution with photoexcited digital graph (360 nm UV light) in the inset.

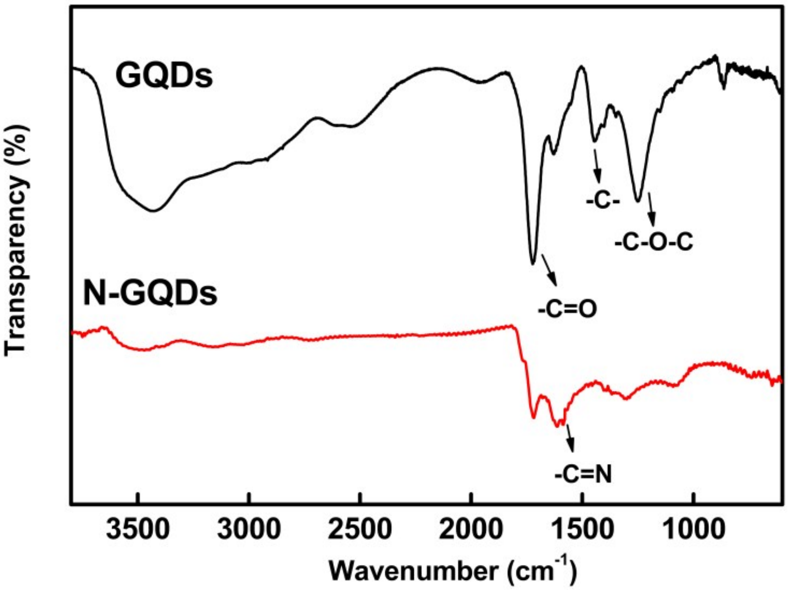

Fig. S3. FT-IR spectra of GQDs and N-GQDs.

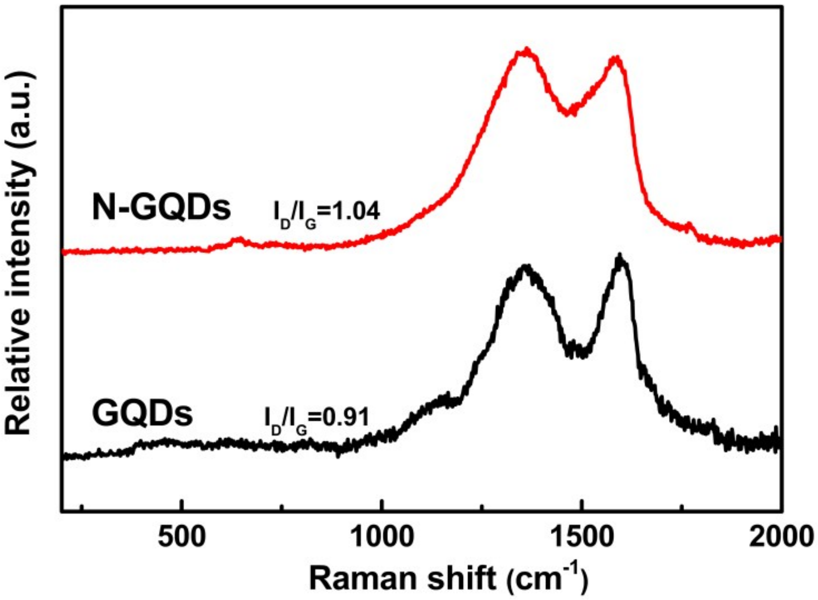

Fig. S4 Raman spectra of GQDs and N-GQDs.

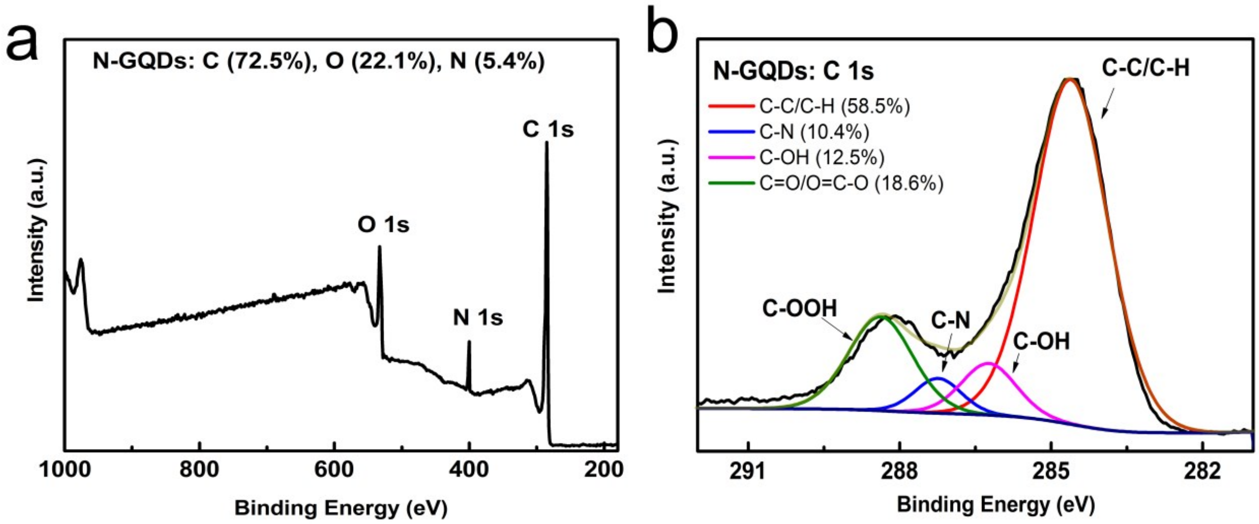

Fig. S5 (a) Survey and (b) high resolution C 1s spectra of N-GQDs.

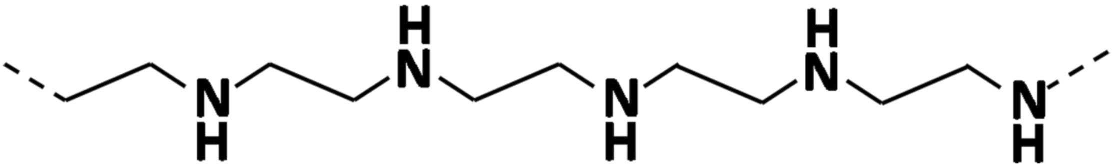

Fig. S6 Molecular structure of polyethylenimine (PEI, $(C_2H_5N)_n$).

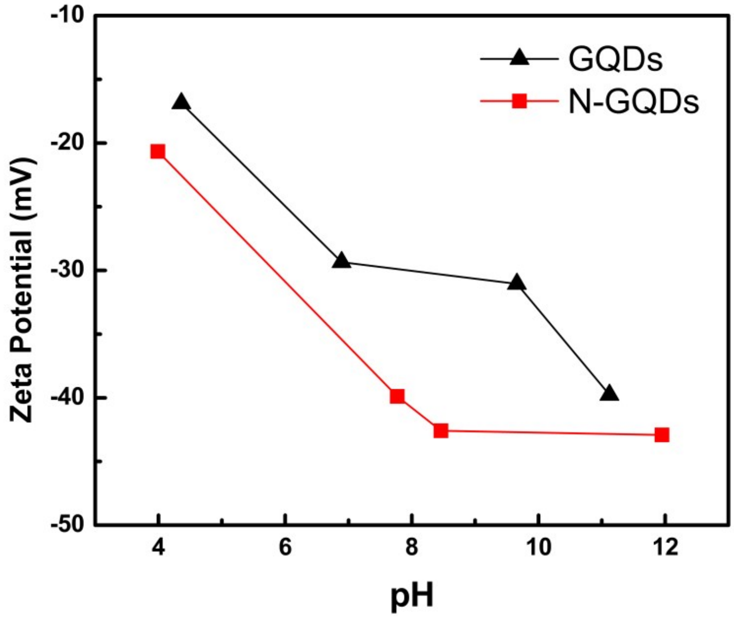

Fig. S7 Zeta potentials of GQDs and N-GQDs aqueous solutions (1.0 mg/mL) as a function of pH value.

Note: Both GQDs and N-GQDs aqueous solutions exhibit negatively charged surfaces within wide pH profile ranging from 4 to 12. The pronounced negatively charge properties of GQDs and N-GQDs aqueous solutions afford a stable aqueous dispersion, which is beneficial for LbL assembly buildup.

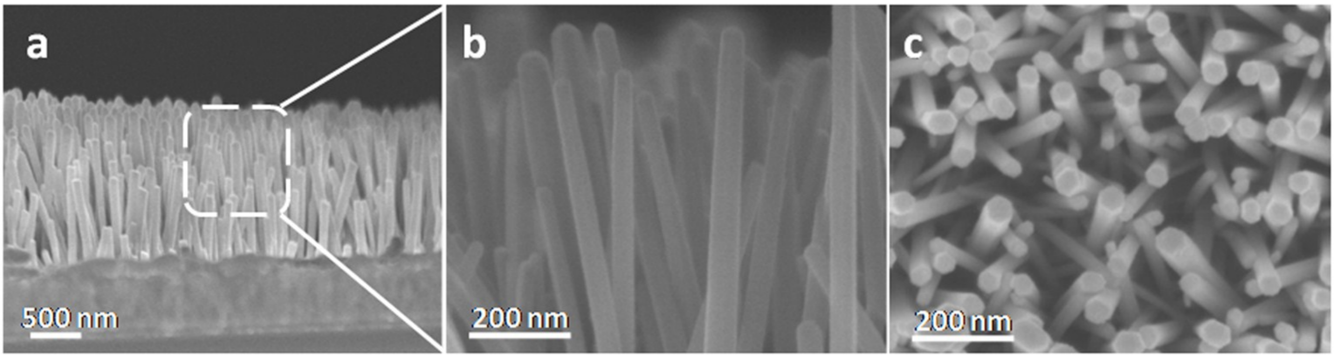

Fig. S8 Cross-sectional (a & b) and (c) top-view FESEM images of ZnO NWs.

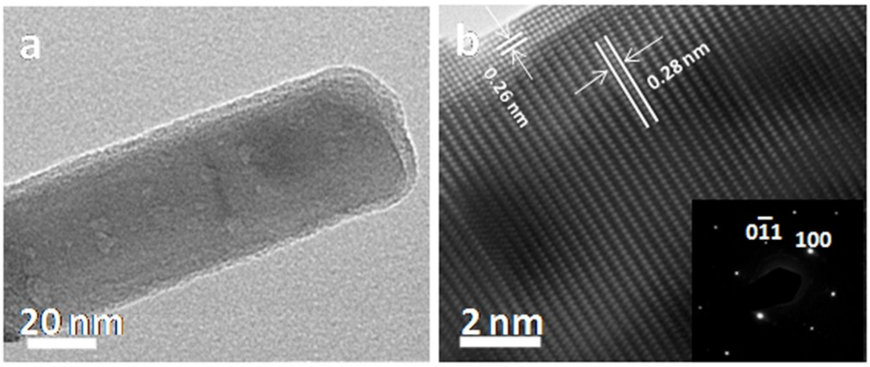

Fig. S9 (a) TEM, and (b) HRTEM image (with a SAED pattern in the inset) of ZnO NWs.

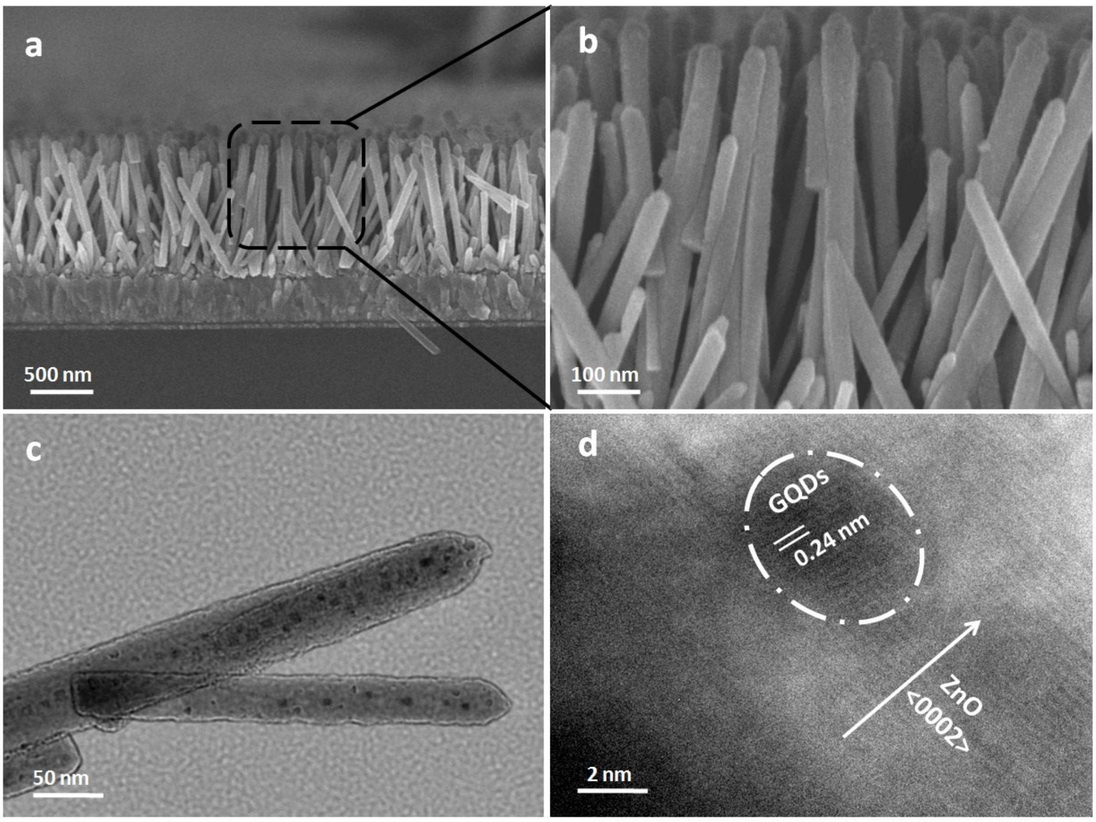

Fig. S10 (a & b) Cross-sectional FESEM images of GQDs/ZnO NWs heterostructure (one assembly layer), (c) TEM and (d) HRTEM images of GQDs/ZnO NWs heterostructure (one assembly layer).

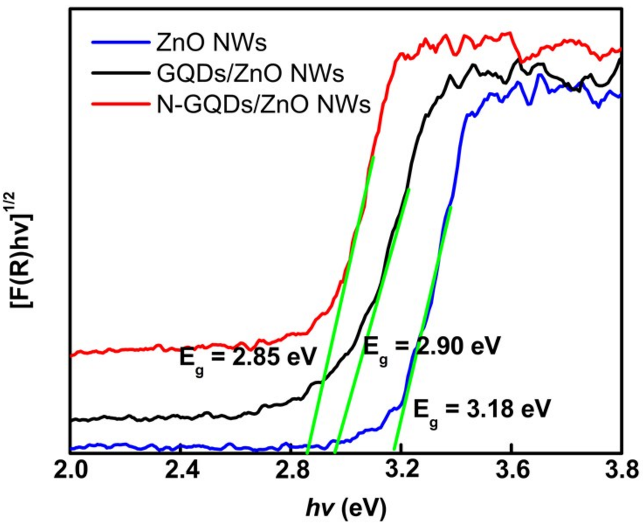

Fig. S11 Plots of transformed Kubelka-Munk function *versus* the energy of light for ZnO NWs, GQDs/ZnO NWs and N-GQDs/ZnO NWs heterostructures (one assembly layer).

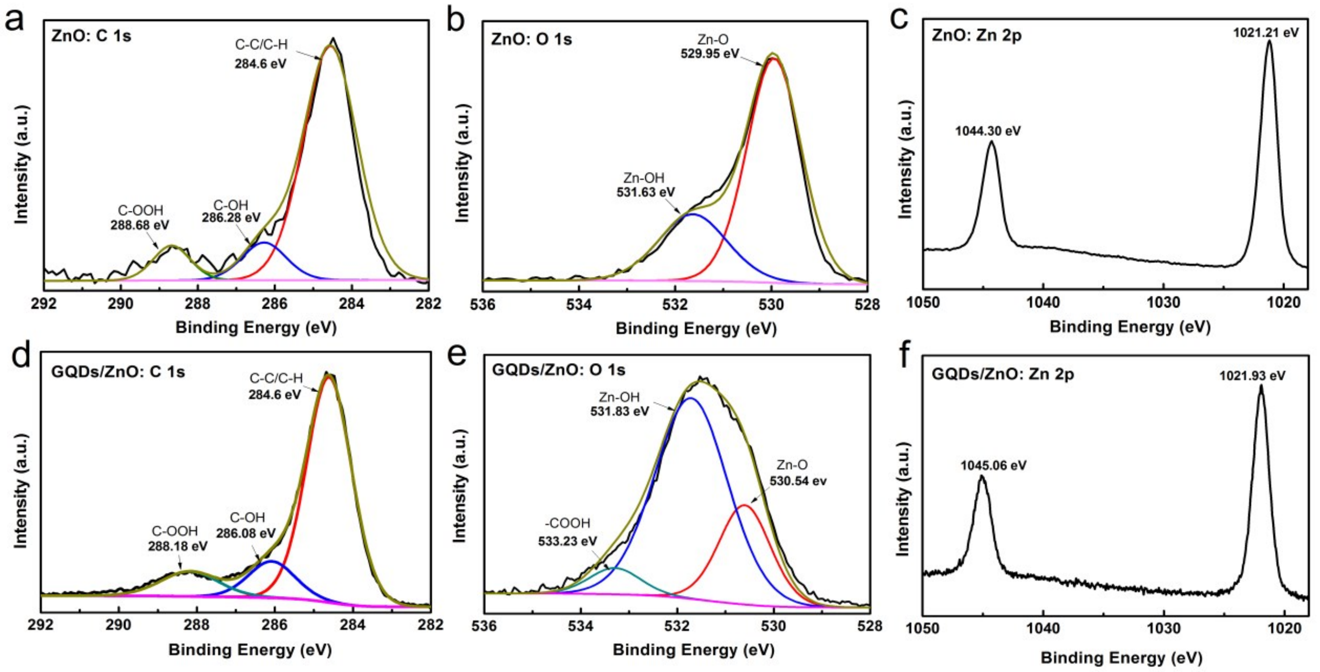

Fig. S12 High-resolution (a) C 1s, (b) O 1s and (c) Zn 2p spectra of ZnO NWs. High-resolution (d) C 1s, (e) O 1s and (f) Zn 2p spectra of GQDs/ZnO NWs heterostructure (one assembly layer).

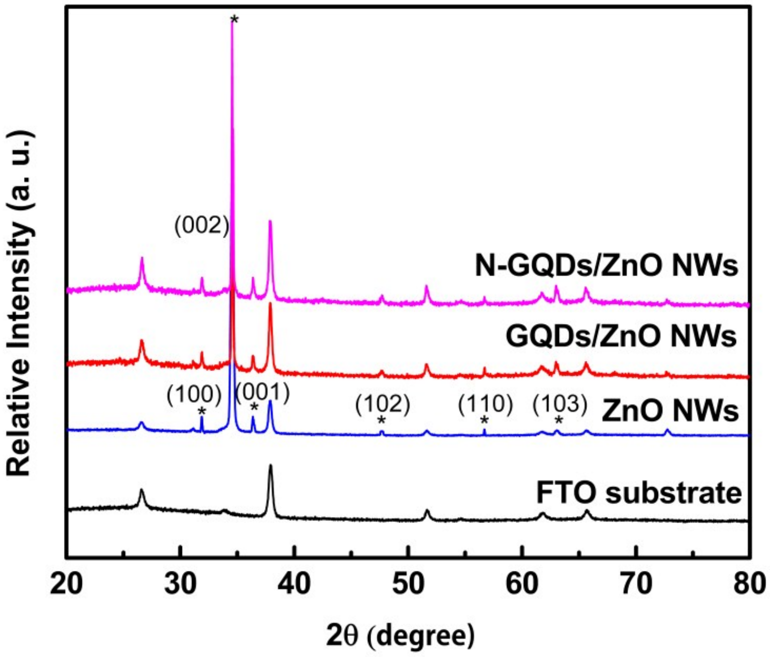

Fig. S13 XRD patterns of ZnO NWs, GQDs/ZnO NWs heterostructure (one assembly layer) and N-GQDs/ZnO NWs heterostructure (one assembly layer).

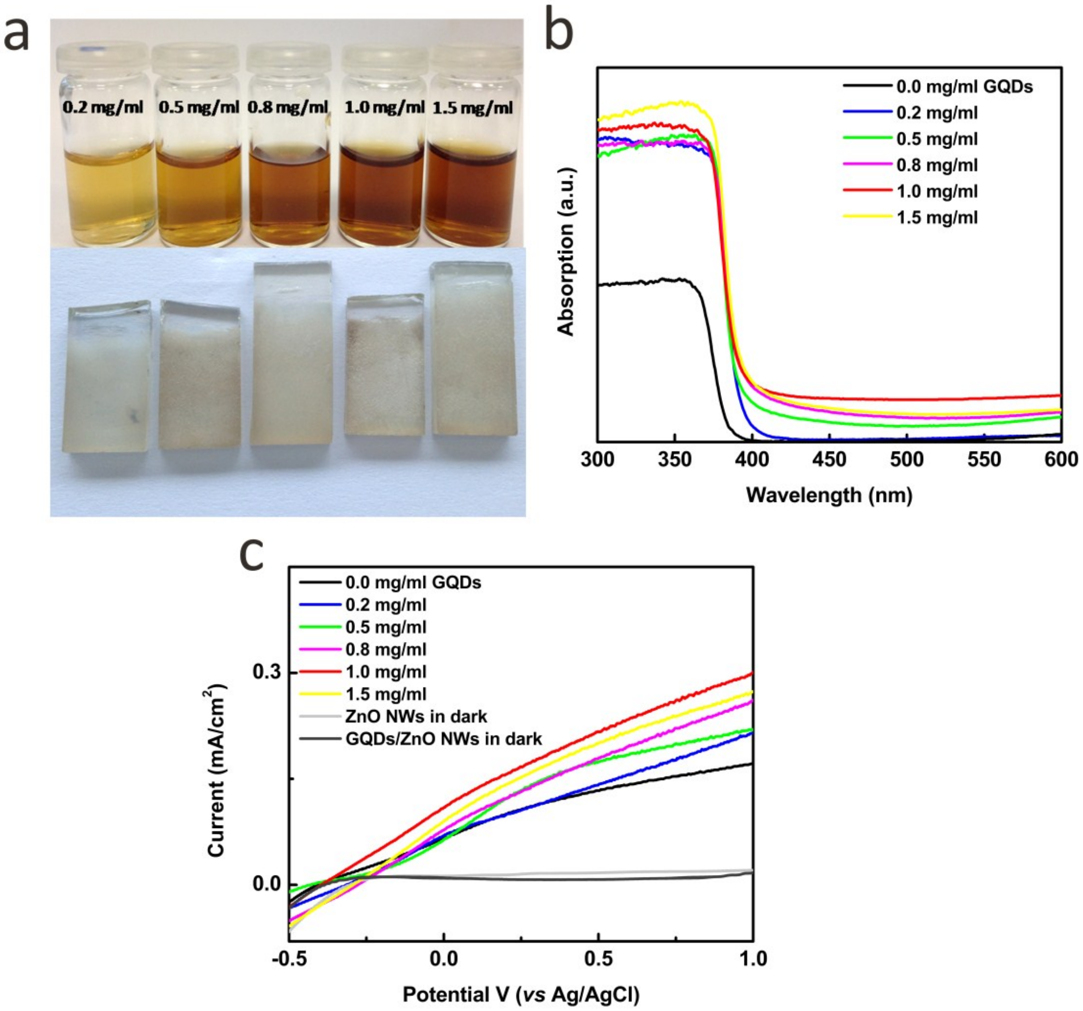

Fig. S14 (a) Photograph of GQDs aqueous solutions with different concentrations and GQDs/ZnO NWs heterostructure fabricated with these GQDs aqueous solutions, (b) UV-vis diffuse reflectance spectra (DRS) and (c) light-responsive linear-sweep voltammograms (LSV) curves of GQDs/ZnO NWs heterostructures in a 0.5 M Na_2SO_4 (pH = 7.34) aqueous solution under simulated solar light irradiation (100 mV cm^{-2}).

Note: GQDs aqueous solutions with different concentrations (from 0.2 to 1.5 mg/mL) were utilized to fabricate GQDs/ZnO NWs heterostructures (one layer), and the results show that absorption intensities and photocurrents of GQDs/ZnO NWs heterostructures increase with the increase of GQDs concentration from 0.2 to 1.0 mg/mL. However, photocurrent of GQDs/ZnO NWs heterostructure decreases when larger GQDs concentration (1.5 mg/mL) was used. Therefore, the optimal GQDs concentration is determined to be1.0 mg/mL.

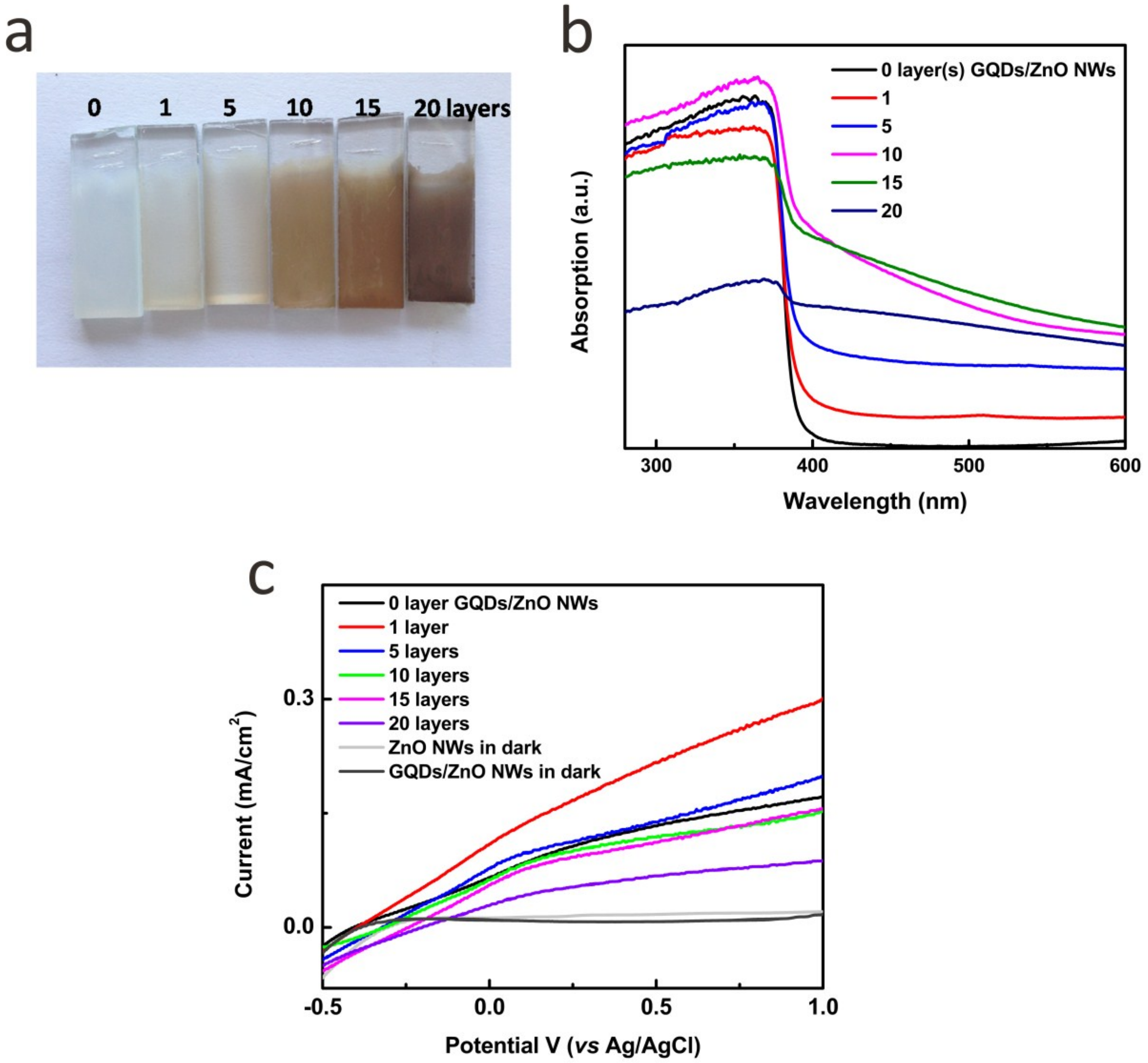

Fig. S15 (a) Photographs, (b) UV-vis diffuse reflectance spectra (DRS), and (c) LSV curves of GQDs/ZnO NWs heterostructures with different assembly layers of GQDs in a 0.5 M Na_2SO_4 (pH = 7.34) aqueous solution under simulated solar light irradiation (100 mW cm^{-2}).

Note: Different assembly layers of GQDs (from 1 to 20 layers, 1.0 mg/mL) were constructed on the ZnO NWs, and DRS as well as PEC performances of GQDs/ZnO NWs heterostructures were probed. The results indicate that absorption intensities of GQDs/ZnO NWs heterostructures increase with the increase of assembly layer from 1 to 10 layers. When the assembly layers is larger than 10 layers, absorption intensities of GQDs/ZnO NWs heterostructures decreases remarkably. Similarly, photocurrent of GQDs/ZnO NWs heterostructures decrease with the assembly layers increasing, which may be mainly due to the aggregation of GQDs on ZnO NWs. Thus, the optimal assembly layer for GQDs is determined to be one layer.

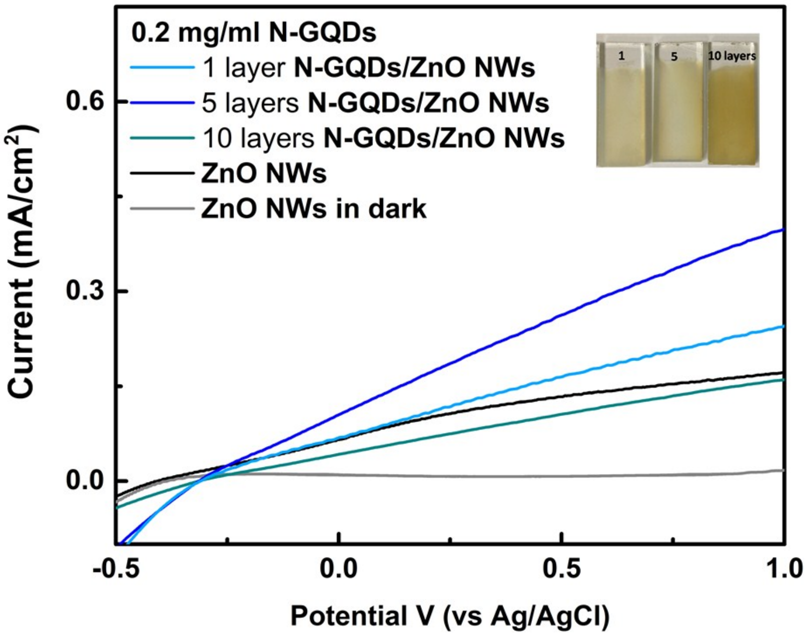

Fig. S16 Current density *versus* applied voltage curves of ZnO NWs, and N-GQDs/ZnO NWs heterostructures with different assembly layers (using 0.2 mg/mL N-GQDs aqueous solutions). PEC measurements of the samples were conducted in a 0.5 M Na_2SO_4 (pH=7.34) aqueous solution under simulated solar light irradiation (100 mW cm^{-2}).

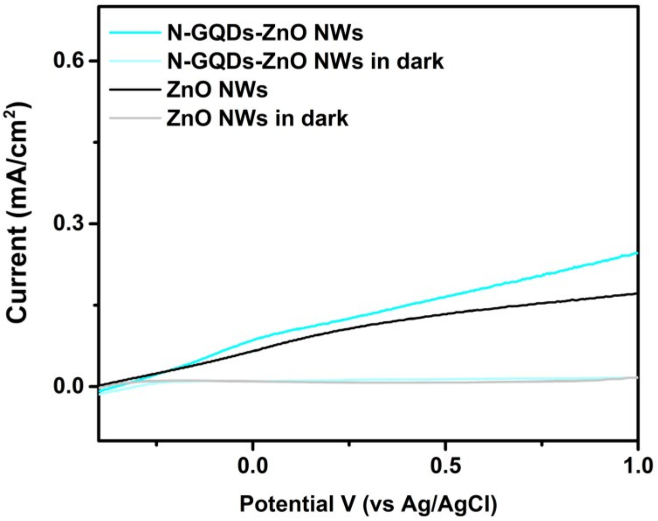

Fig. S17 LSV curves of N-GQDs modified ZnO NWs nanocomposites prepared by a conventional coating method. PEC performances of the samples were explored in a 0.5 M Na_2SO_4 (pH=7.34) aqueous solution under simulated solar light irradiation (100 mW cm^{-2}).

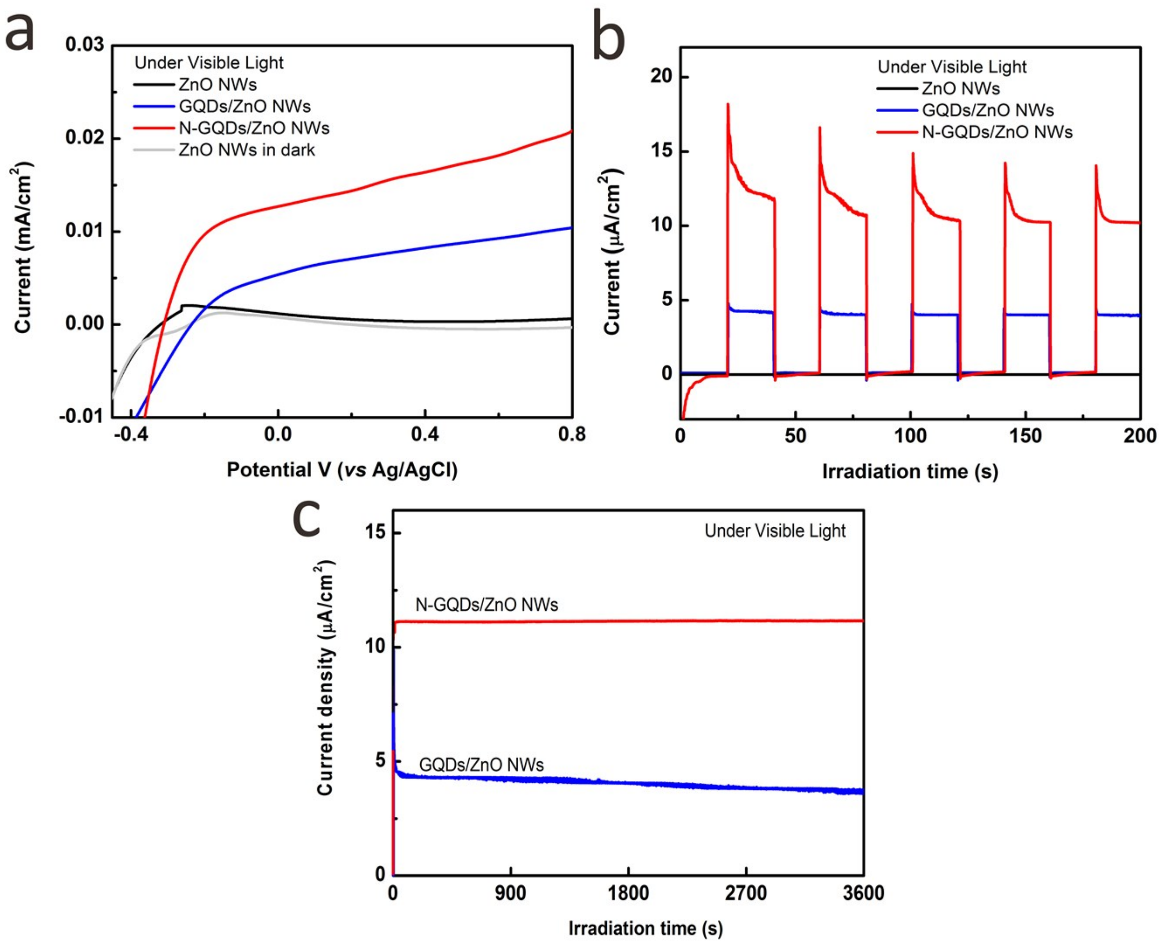

Fig. S18 (a) Current density *versus* applied voltage curves, (b) transient photocurrent responses of ZnO NWs, GQDs/ZnO NWs (one assembly layer, 1.0 mg/mL GQDs) and N-GQDs/ZnO NWs (one assembly layer, 1.0 mg/mL N-GQDs), and (c) photostability of GQDs/ZnO NWs and N-GQDs/ZnO NWs heterostructures (one assembly layer) in a 0.5 M Na_2SO_4 (pH=7.34) aqueous solution with zero bias *versus* Ag/AgCl under visible light irradiation (λ > 420 nm).

Note: LSV results of different samples under visible light irradiation indicate that N-GQDs/ZnO heterostructure exhibits the most superior photocurrent as compared with ZnO NWs and GQDs/ZnO NWs counterparts (**Fig. S17a**). Consistently, periodic on/off transient photocurrent responses of different samples under intermittent visible light irradiation in **Fig. S17b** demonstrate the same trend. Alternatively, as shown in **Fig. S17c**, N-GQDs/ZnO NWs and GQDs/ZnO NWs heterostructures demonstrate favorable photostability under continuous visible light irradiation for 1 h, which is analogous to photostability of composite nanostructures under simulated solar light irradiation.

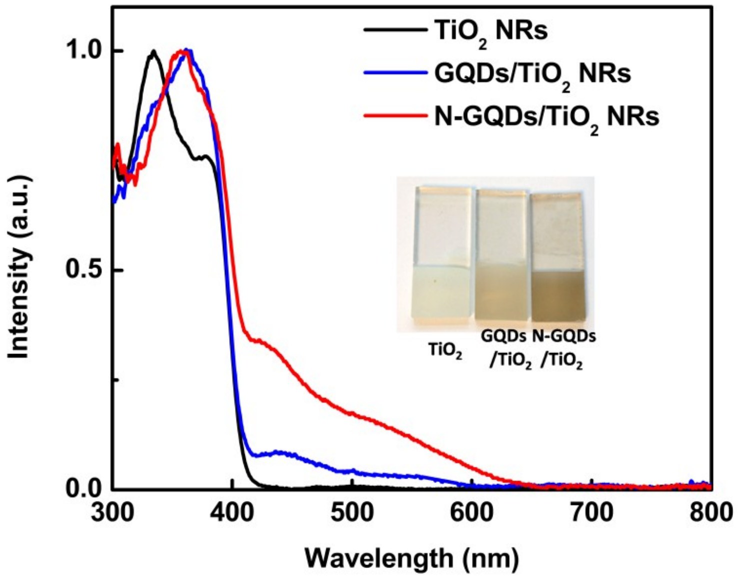

Fig. S19 UV-vis diffuse reflectance spectra (DRS) of TiO_2 NRs, GQDs/TiO_2 NRs (one assembly layer) and N-GQDs/TiO_2 NRs heterostructure (one assembly layer).

Note: Analogous to DRS results of ZnO NWs based composites, N-GQDs/TiO_2 NRs and GQDs/TiO_2 NRs heterostructures exhibit pronounced absorption in visible region, while no absorption in the same wavelength region was observed for TiO_2 NRs, indicating the pivotal role of N-GQDs and GQDs as photosensitizers. Moreover, it is worthwhile that N-GQDs/TiO_2 NRs heterostructures demonstrates significantly enhanced light absorption in visible region as compared with GQDs/TiO_2 NRs counterpart with the same assembly layer, which highlights the contributing role of nitrogen doping in boosting light absorption of GQDs and GQDs/TiO_2 NRs heterostructure.

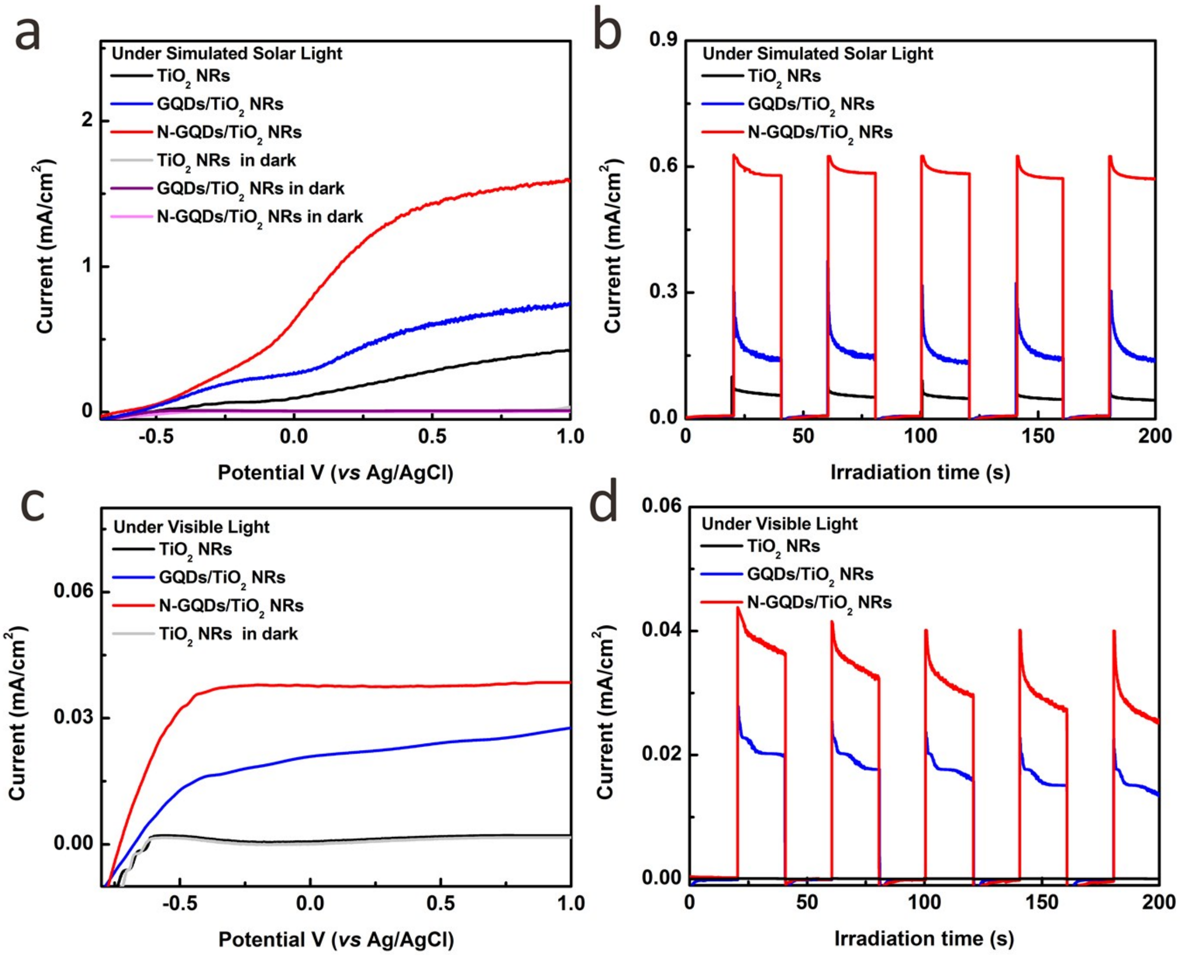

Fig. S20 (a, c) Current density *versus* applied voltage curves, and (b, d) transient photocurrent responses of TiO_2 NRs, GQDs/TiO_2 NRs and N-GQDs/TiO_2 NRs heterostructures (using 1.0 mg/mL GQDs and N-GQDs aqueous solutions with one assembly layer). The PEC measurements were carried out in a 0.5 M Na_2SO_4 aqueous solution (pH = 7.34) under simulated solar or visible light irradiation (100 mW cm^{-2}).

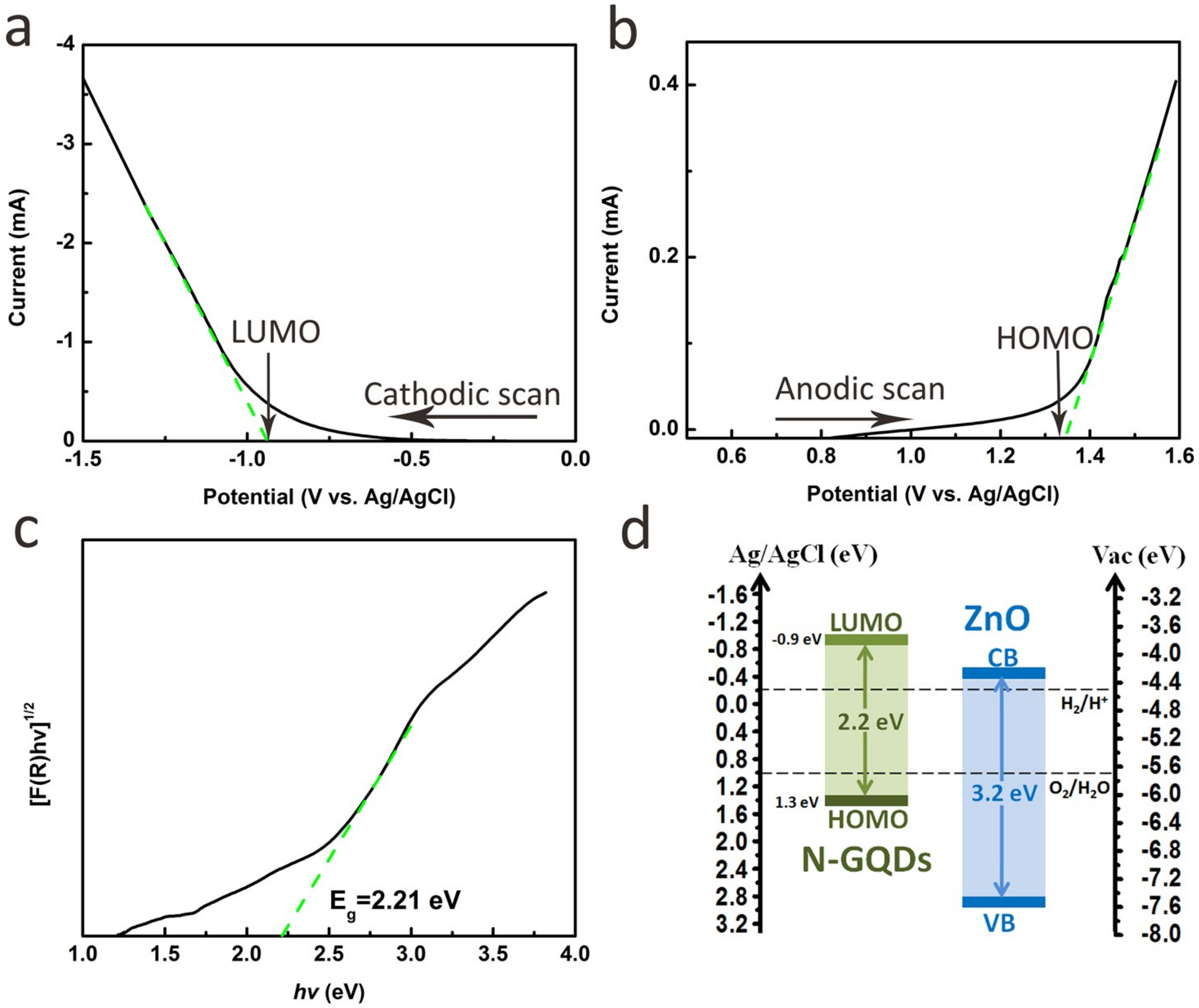

Fig. S21 (a) Cathodic scan to indentify the LUMO energy level of N-GQDs with a rate of 5 mV/s, and (b) anodic scan to indentify the HOMO energy level of N-GQDs with a rate of 5 mV/s. (c) Plots of transformed Kubelka-Munk function *versus* the energy of light for N-GQDs. (d) Schematic illustration of energy levels of N-GQDs and ZnO NWs.

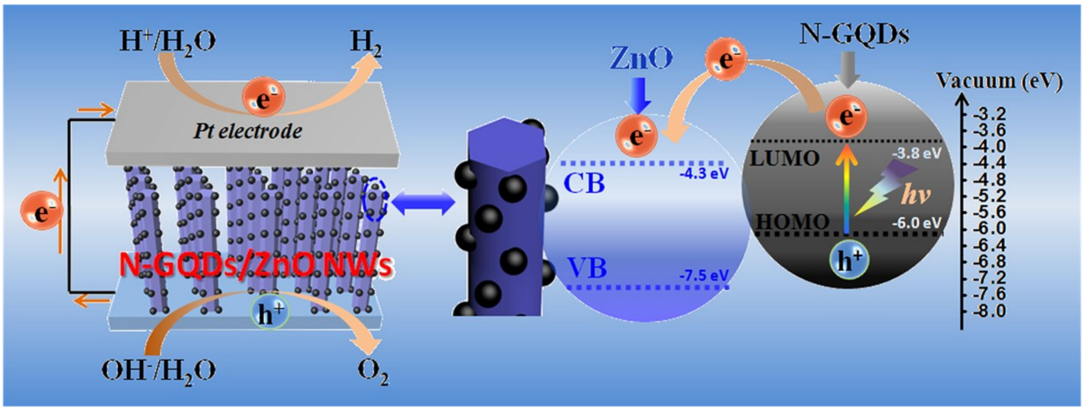

Fig. S22 Schematic illustration of PEC water splitting mechanism over N-GQDs/ZnO NWs heterostructure under visible light irradiation.